# Supporting Information

## Push-Pull benzophenone derivatives based visible photoinitiating systems: synthesis, characterization, properties, and application for LED free radical photopolymerization

Qingqing Wu*[1], Jingdong Guo[1], Mingsen Deng[2], Fushao Li[1].

[1]*Guizhou Provincial Key Laboratory of Computational Nano-Material Science, Guizhou Education University, Guiyang 550018, PR China*

[2]*Laboratory for Solid-State Energy Storage and Intelligent System (SESIS-Lab), School of Information, Guizhou University of Finance and Economics, Guiyang, Guizhou 550025, PR China.*

* Corresponding authors.

E-mail: 2011202030085@whu.edu.cn (Q. Wu)

## 1. Experimental Section

### 1.1 Materials

(4-Amino-3-nitrophenyl)(phenyl)methanone (99%, RG), benzyl bromide (99%, RG), 4-tert-butylbenzyl bromide (99%+, RG), 4-iodobenzyl bromide (98%+, RG), 4-(trifluoromethyl)benzyl bromide (98%, RG), diphenyl(2,4,6-trimethylbenzoyl)phosphine oxide(TPO, 98%+, RG), 2-isopropylthioxanthone (ITX, 98%+, RG), benzophenone (BP, 99%, RG), acetonitrile (99.5%, AR), potassium carbonate (99.99%, RG) and potassium iodide (99%, RG) were purchased from Adamas (Shanghai, China). Ethyl 4-dimethylaminobenzoate (EDB, 99%, RG), bis(4-tert-butylphenyl) iodonium hexafluorophosphate (Iod, 98%, RG), tert-butylbenzene (98%, RG) and N-benzylidene-2-methylpropan-2-amine oxide (PBN, 99%, RG) were purchased from Admas (Shanghai, China). 1, 6-Hexanediol diacrylate (HDDA, 90% stabilized with MEHQ 100ppm) was purchased from Heowns (Tianjin, China).

### 1.2 Synthesis and characterization

The synthesis route is shown in Scheme 2. The (4-benzylamino-3-nitrophenyl)(phenyl)methanone derivatives were prepared by the nucleophilic substitution between (4-Amino-3-nitrophenyl)(phenyl)methanone and benzyl bromide. The obtained structure was recorded using a nuclear magnetic resonance spectrometer (Bruker 400MHz NMR spectrometer) with $CDCl_3$ as a solvent. HRMS spectra were obtained using a Bruker maxis impact high resolution mass spectrometer with chromatography-pure methanol as a solvent.

Synthesis of (4-benzylamino-3-nitrophenyl)(phenyl)methanone (**BP-NB**): (4-Amino-3-nitrophenyl)(phenyl)methanone (0.242 g, 1.0 mmol), benzyl bromide (0.188g, 1.1 mmol) and $K_2CO_3$ (0.152g, 1.1mmol) were added to the solvent acetonitrile (10 mL) in a round bottom flask. The process was monitored by thin layer chromatography (TLC). The mixture was stirred for 72 h at room temperature. After this, a yellow solid was obtained by filtration and washing with water, ethanol.

$^1H$ NMR ($CDCl_3$, 400 MHz, δ): 4.61-4.68 (2H, d, J=9.2Hz), 6.90-6.97 (1H, d, J=9.2Hz), 7.30-7.43 (5H, m), 7.45-7.53 (2H, m), 7.55-7.63 (1H, m), 7.70-7.77 (2H, m), 7.96-8.03 (1H, dd, J=1.6Hz, J=9.2Hz), 8.67-8.72 (1H, d, J=2.0 Hz), 8.75-8.84 (1H, m); $^{13}C$ NMR ($CDCl_3$, 101 MHz, δ): 193.57 (C=O), 147.53, 137.53, 137.07, 136.35, 132.29, 131.24, 130.69, 129.51, 129.16, 128.51, 128.11, 127.10, 125.10, 114.30, 47.33 ($CH_2$). HRMS (ESI) calculated for $C_{20}H_{16}N_2O_3$, 355.1053, [M + nNa],

found 355.1053.

BP-NBI, BP-NBtBu and BP-NBCF$_3$ were synthesized by the same preparation method described as the synthesis of BP-NB.

**BP-NBI** : $^1$H NMR ($CDCl_3$, 400 MHz, δ): 4.55-4.61 (2H, d, J=6.0Hz), 6.82-6.89 (1H, d, J=9.2Hz), 7.06-7.14 (2H, d, J=8.4Hz), 7.44-7.53 (2H, m), 7.55-7.64 (1H, m), 7.67-7.77 (4H, m), 7.94-8.01 (1H, dd, J=1.6Hz, J=9.2Hz), 8.66-8.72 (1H, d, J=1.6 Hz), 8.74-8.82 (1H, m); $^{13}$C NMR ($CDCl_3$, 101 MHz, δ): 193.45 (C=O), 147.25, 138.19, 137.39, 137.10, 136.11, 132.32, 131.37, 130.57, 129.48, 128.88, 128.50, 125.34, 114.14, 93.43, 46.74 ($CH_2$). HRMS (ESI) calculated for $C_{20}H_{15}IN_2O_3$ 459.0200, [M + nH], found 459.0200.

**BP-NBtBu**: $^1$H NMR ($CDCl_3$, 400 MHz, δ): 1.33 (9H, s), 4.55-4.63 (2H, d, J=5.6 Hz), 6.92-7.01 (1H, d, J=8.8 Hz), 7.22-7.31 (m, 2H), 7.36-7.45 (2H, m), 7.46-7.53 (2H, m), 7.55-7.63 (1H, m), 7.67-7.77 (2H, m), 7.97-8.04 (1H, dd, J=1.6Hz, J=9.2Hz), 8.66-8.71 (1H, d, J=2.0 Hz), 8.72-8.80 (1H, m); $^{13}$C NMR ($CDCl_3$, 101 MHz, δ): 193.56(C=O), 151.17, 147.55, 137.54, 137.02, 133.22, 132.23, 131.09, 130.69, 129.48, 128.48, 126.92, 126.04, 124.93, 114.32, 47.04 ($CH_2$), 34.60 (**C**$(CH_3)_3$), 31.31($CH_3$); HRMS (ESI) calculated for $C_{24}H_{24}N_2O_3$ 389.1860, [M + nH], found 389.1806.

**BP-NBCF$_3$**: $^1$H NMR ($CDCl_3$, 400 MHz, δ): 4.69-4.74 (2H, d, J=5.6Hz), 6.80-6.88 (1H, d, J=9.2Hz), 7.44-7.53 (4H, m), 7.55-7.63 (1H, m), 7.63-7.69 (2H, m), 7.70-7.76 (2H, m), 7.96-8.02 (1H, dd, J=1.6Hz, J=9.2Hz), 8.69-8.73 (1H, d, J=1.6Hz), 8.80-8.92 (1H, t, J=4.8Hz); $^{13}$C NMR ($CDCl_3$, 101 MHz, δ): 193.45(C=O), 147.23, 140.57, 137.37, 137.20, 132.39, 131.52, 130.58, 130.24, 129.51, 128.53, 127.22, 126.15, 125.56, 125.27, 114.09, 46.76 ($CH_2$). HRMS (ESI) calculated for $C_{21}H_{15}F_3N_2O_3$ 401.1108, [M + nH], found 401.1108.

**1.3 UV-visible spectroscopy, fluorescence characteristics and photolysis experiments**

For the UV-visible spectroscopy and photolysis experiments, the sample concentration was [BP-NBR]= $1.5\times10^{-4}$mol/L; [EDB] = [Iod] = $3\times10^{-3}$mol/L in acetonitrile. The absorption spectrum of different systems in acetonitrile was measured by a Perkin Elmer Lambda 365 spectrophotometer. For the photolysis experiments, we monitored their changes in the UV-vis absorption spectrum when irradiated under 405 nm LED (irradiation intensity = 65 mW cm$^{-2}$) at different times. The UV-visible absorption spectra experiment and the photolysis experiment were repeated three times, with each error being below 0.01, and the average value was calculated. Fluorescence spectra were measured

using an Agilent Cary Eclipse spectrophotometer, and acetonitrile was used as the solvent.

**1.4 Photopolymerization experiments**

The photopolymerization kinetic experiments were conducted by real-time FT-IR spectroscopy (Perkin Elmer Spectrum Two) at 20℃. It was recorded to detect the conversion of the double bond of HDDA with the change of time upon the LEDs exposure. The following LEDs were used as irradiation sources: LED@405 nm with an incident light intensity at the sample surface: I=120 mW $cm^{-2}$. LED@435 nm, I=110 mW $cm^{-2}$, LED@450 nm, I=140 mW $cm^{-2}$. The irradiance intensity is tested by irradiatometer (NBeT: NEBT19011). The weight percent of the different chemical compounds of the photoinitiating system is calculated from the monomer content (w/w). The molar ratio of the photoinitiating system is calculated from the monomer content (mol/g). The homogenous liquid sample was spread evenly between two KBr pellets. The irradiation starts at time=7s. All the irradiation time is 300s for one sample. By monitoring the variation of C=C absorption peak areas of 1580-1650$cm^{-1}$, the change of double band conversion over time was determined. The formula is shown below

$$Conversion(\%) = \frac{A_0 - A_t}{A_0} \times 100\%$$

where $A_0$, $A_t$ represents the area of double bond before irradiation and after irradiation at testing time t, respectively. The experiment was repeated until the standard deviation of the conversion measurements over time was less than 2%, ensuring the reliability and reproducibility of the results. Furthermore, the rate of polymerization ($R_p$) is directly related to the conversion ($d_{Conversion}/dt$) by the equation[1]:

$$R_p = \frac{d_{Conversion}}{dt}$$

**1.5 Density functional theory (DFT) calculations**

In this work, all computational studies have been performed using the Gaussian 16 software (Rev. A. 03)[2]. The molecular geometry of the benzophenone derivatives was optimized using B3LYP functional in combination with 6-311G (d, p) basis sets for C H O N F atom. We have specified that for iodine atoms, given their large atomic number, we employed the def2tzvp basis set. The choice of functional and basis set was shown in the following section. The vibrational frequencies were further examined to ensure the obtained geometries are void of imaginary frequency. Their excited states were also calculated by the same method and basis sets. In all cases

implicit solvent effects were accounted for using the solvation model density (SMD) model of acetonitrile[3]. The charge distribution of ground and excited states and band changes of BP-NBR were analyzed using Multiwfn software[4,5] and VMD software was used to visualize the molecular structure.

**1.6 Cyclic voltammetry experiments to measure the redox potentials**

The Gibbs free energy change for the charge transfer reaction was calculated by the Rehm-Weller equation[6],

$$\Delta G_{et} = E_{OX} - E_{red} - E_{S1} - C$$

where $E_{ox}$ and $E_{red}$ were the oxidation potential of the electron donor and the reduction potential of the electron acceptor, respectively; $E_{S1}$ was the energy of the first excited state. The constant C was the electrostatic energy and was negligible[7].

The cyclic voltammetry measurements were performed using an electrochemical workstation (CH Instruments Model 760E Series electrochemical workstation) to determine the redox potential of the sample. The concentration of the sample was $10^{-3}$ mol/L in acetonitrile. Tetrabutylammonium hexafluorophosphate (0.05 mol/L) was used as a supporting electrolyte. Ferrocene was used as the internal reference. A glassy carbon electrode was used as a working electrode and a saturated calomel electrode (SCE) was used as a reference electrode. A platinum wire electrode was used as a counter electrode. The solutions were previously Ar bubbled for 5 min to eliminate the influence of oxygen. Measurements were performed with a scan rate of 100 mV/s.

**1.7 Electron paramagnetic resonance spin trapping (EPR-ST) experiments**

EPR-ST experiments were carried out using a Bruker magnetech ESR5000. *Tert*-butylbenzene solutions of PI, PI/Iod and PI/EDB (0.01 mol/L) were added to 6 mm quartz cylindrical EPR tube and were deoxygenated with argon 5 min prior to measurements. The radicals were generated at room temperature upon the LED@405 nm exposure and trapped by PBN (≈0.01 mol/L). The EPR spectrum simulations were carried out with biomolecular EPR spectroscopy software. The sweep width was 300.00 G, the sweep time was 60 s, the modulation frequency was 100.00 kHz, and the modulation amplitude was 2.00 G.

**S1.8 Thermogravimetric analysis (TGA)**

The thermal stability of the photoinitiators was assessed using a thermogravimetric analysis technique (NETZSCH TG 209 F1 Libra). The experimental setup included the use of nitrogen both

for purging and as a protective atmosphere, with a flow rate set at 20 ml/min. The temperature was increased at a rate of 10.0 K/min from an initial 30℃ up to a final temperature of 600℃.

## 2. Results and discussion

### 2.1 Characterization

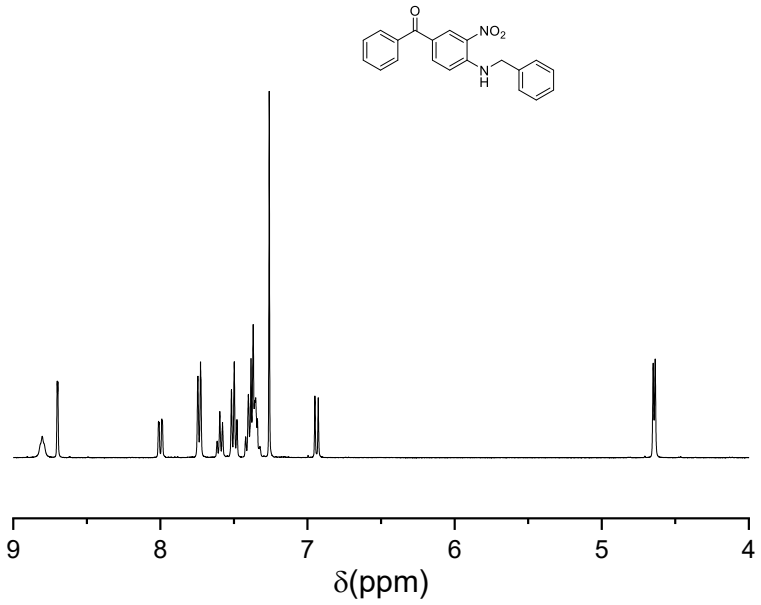


**Fig. S1** The $^{1}H$ NMR spectrum of BP-NB in $CDCl_3$.

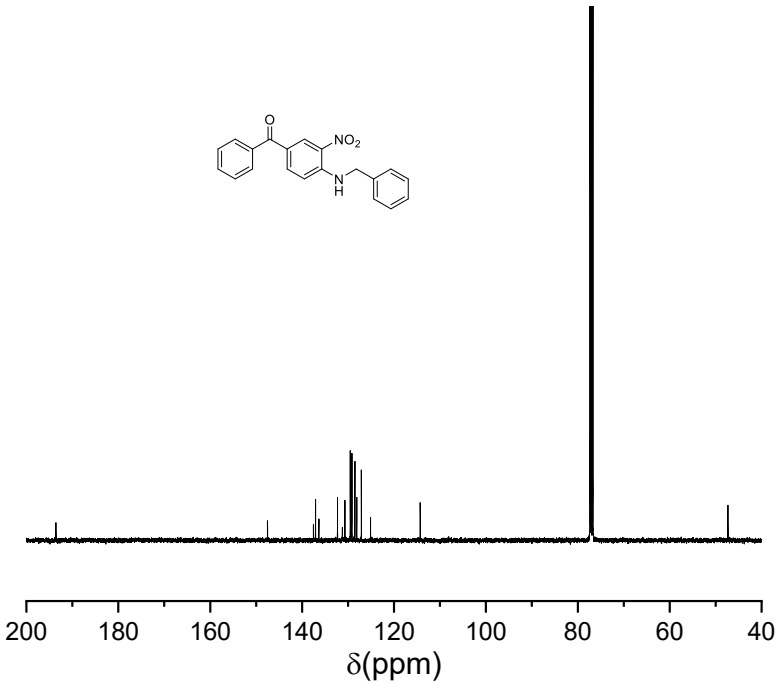


**Fig. S2** The $^{13}C$ NMR spectrum of BP-NB in $CDCl_3$.

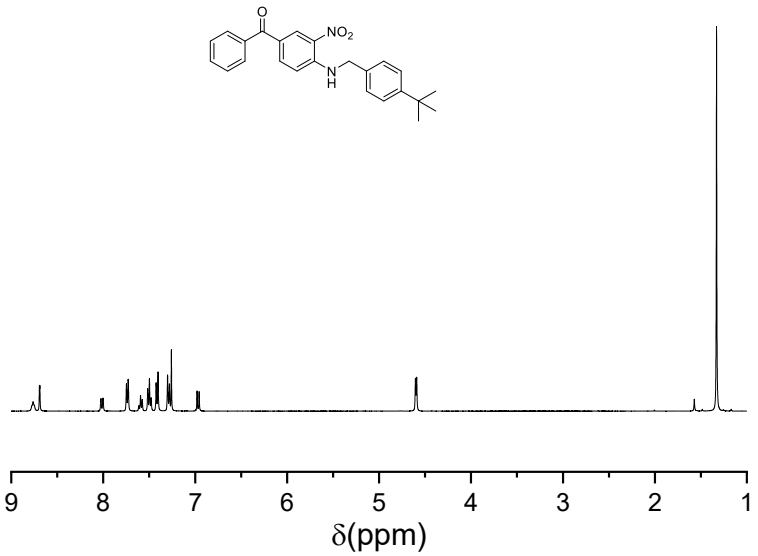


**Fig. S3** The $^{1}H$ NMR spectrum of BP-NBtBu in $CDCl_3$.

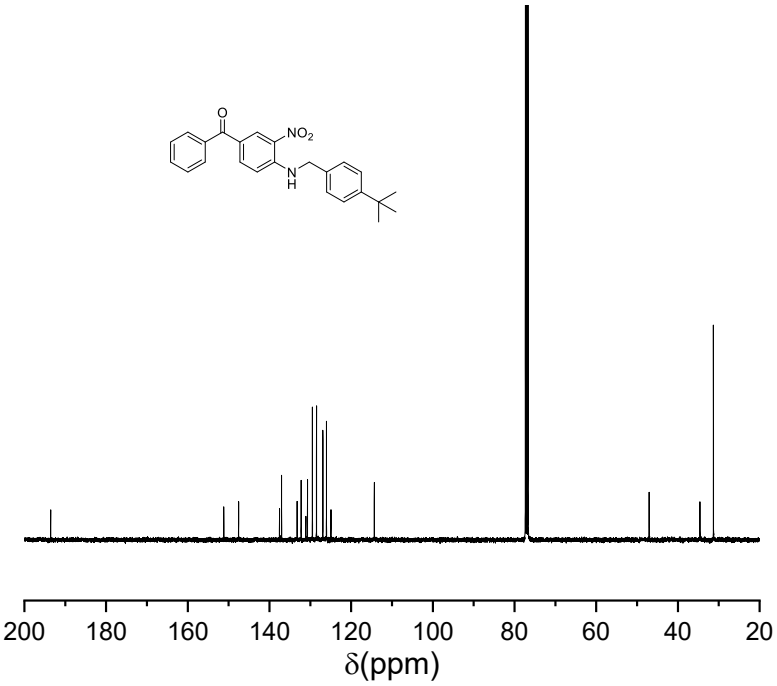


**Fig. S4** The $^{13}C$ NMR spectrum of BP-NBtBu in $CDCl_3$.

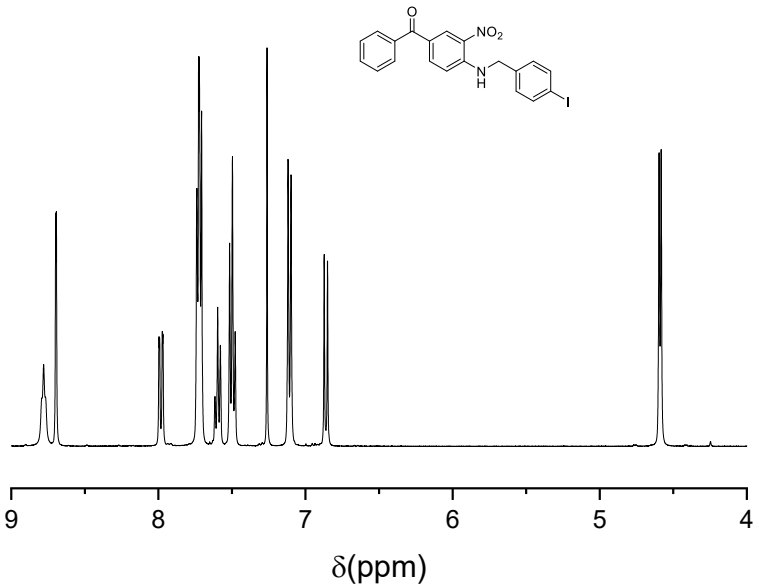


**Fig. S5** The $^{1}H$ NMR spectrum of BP-NBI in $CDCl_3$.

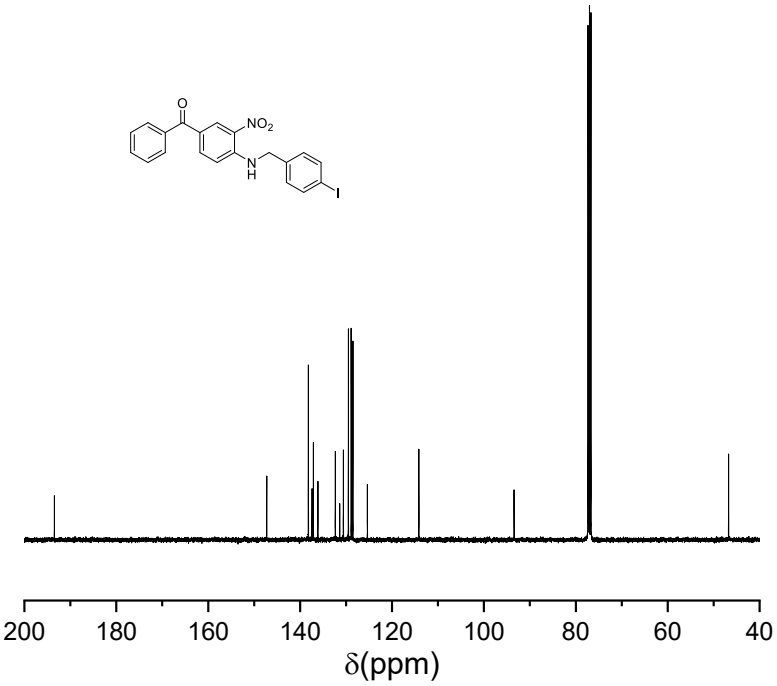


**Fig. S6** The $^{13}C$ NMR spectrum of BP-NBI in $CDCl_3$.

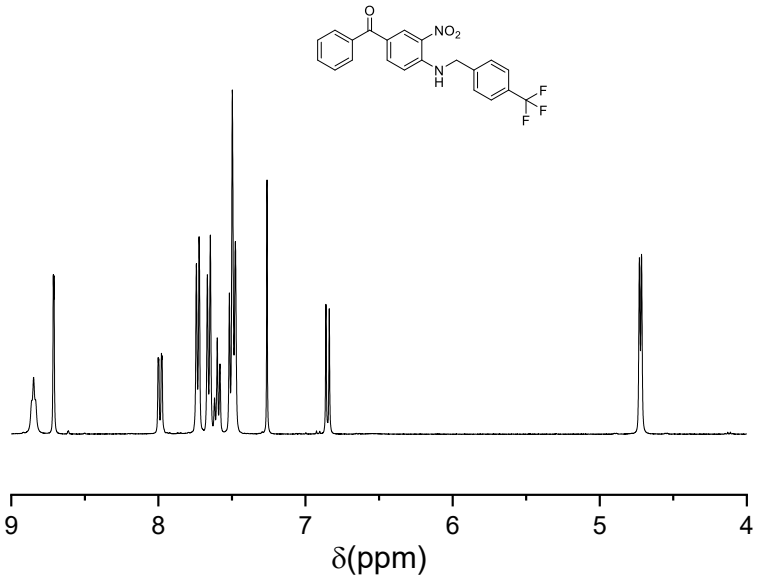


**Fig. S7** The $^{1}H$ NMR spectrum of BP-NBCF$_3$ in CDCl$_3$.

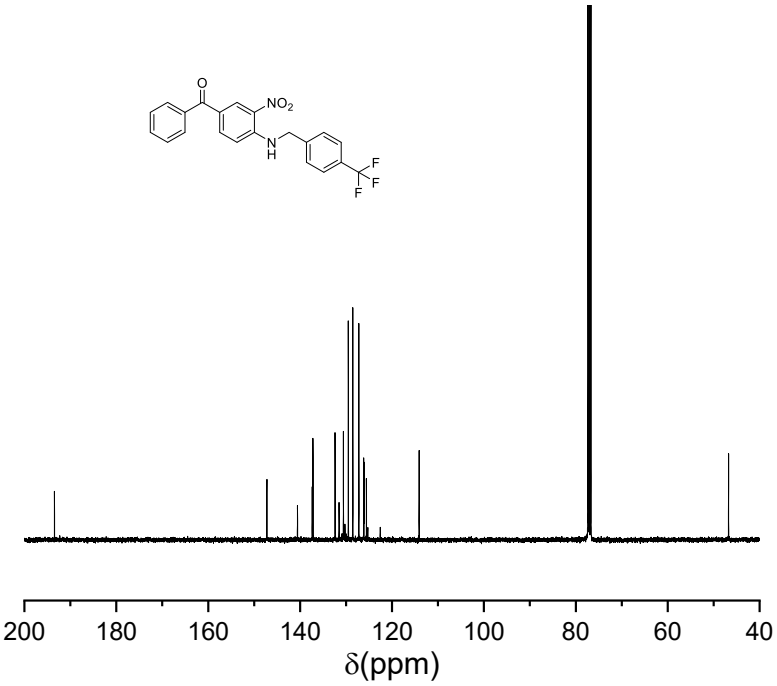


**Fig. S8** The $^{13}C$ NMR spectrum of BP-NBCF$_3$ in CDCl$_3$.

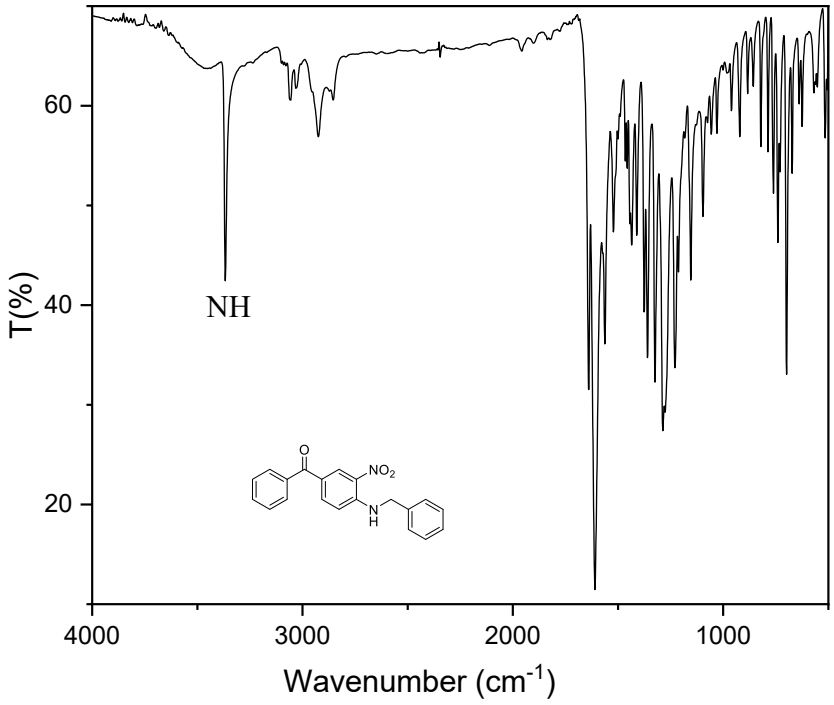


**Fig. S9** The FT-IR spectrum of BP-NB.

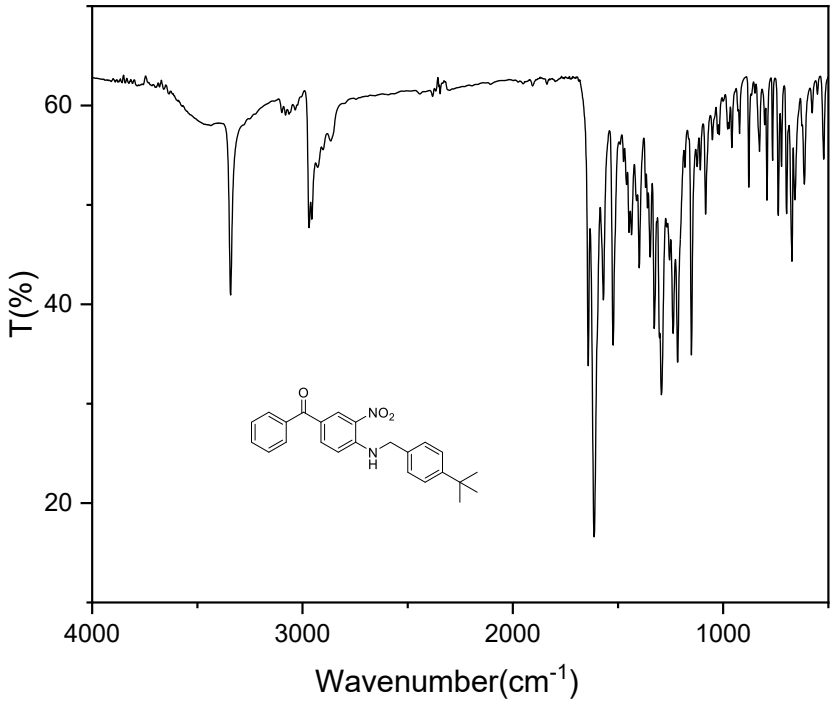


**Fig. S10** The FT-IR spectrum of BP-NBtBu.

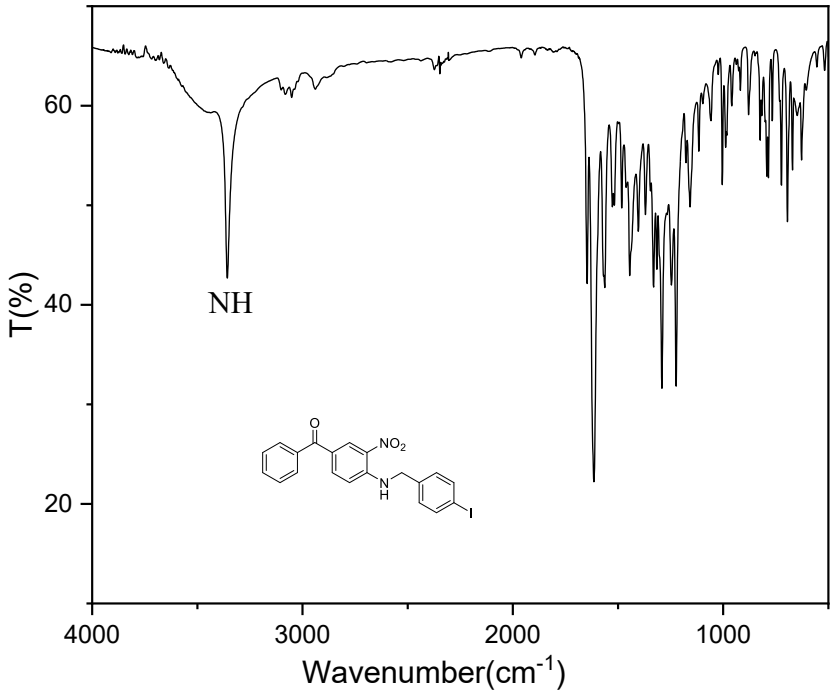


**Fig. S11** The FT-IR spectrum of BP-NBI.

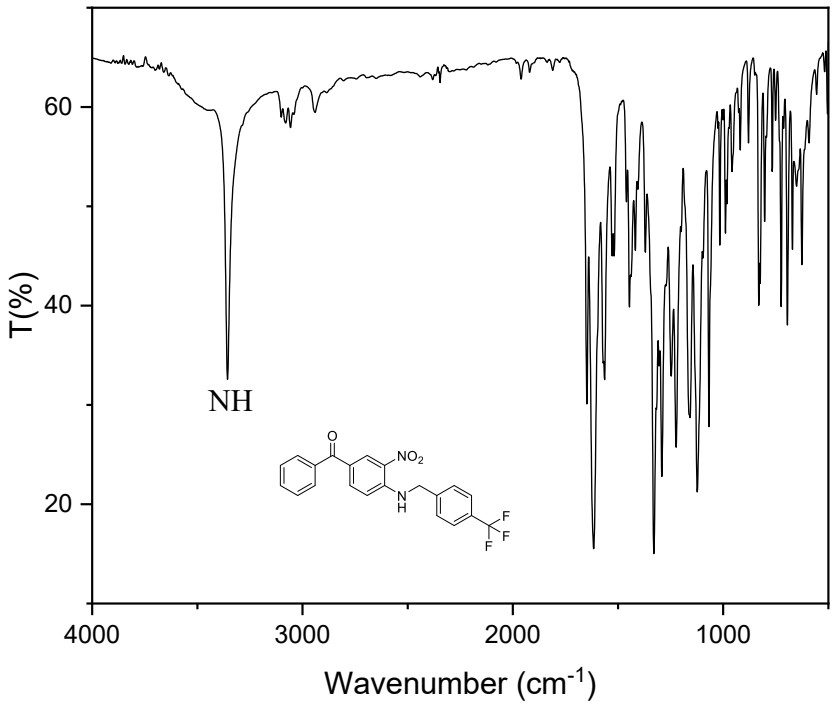


**Fig. S12** The FT-IR spectrum of BP-NBCF$_3$.

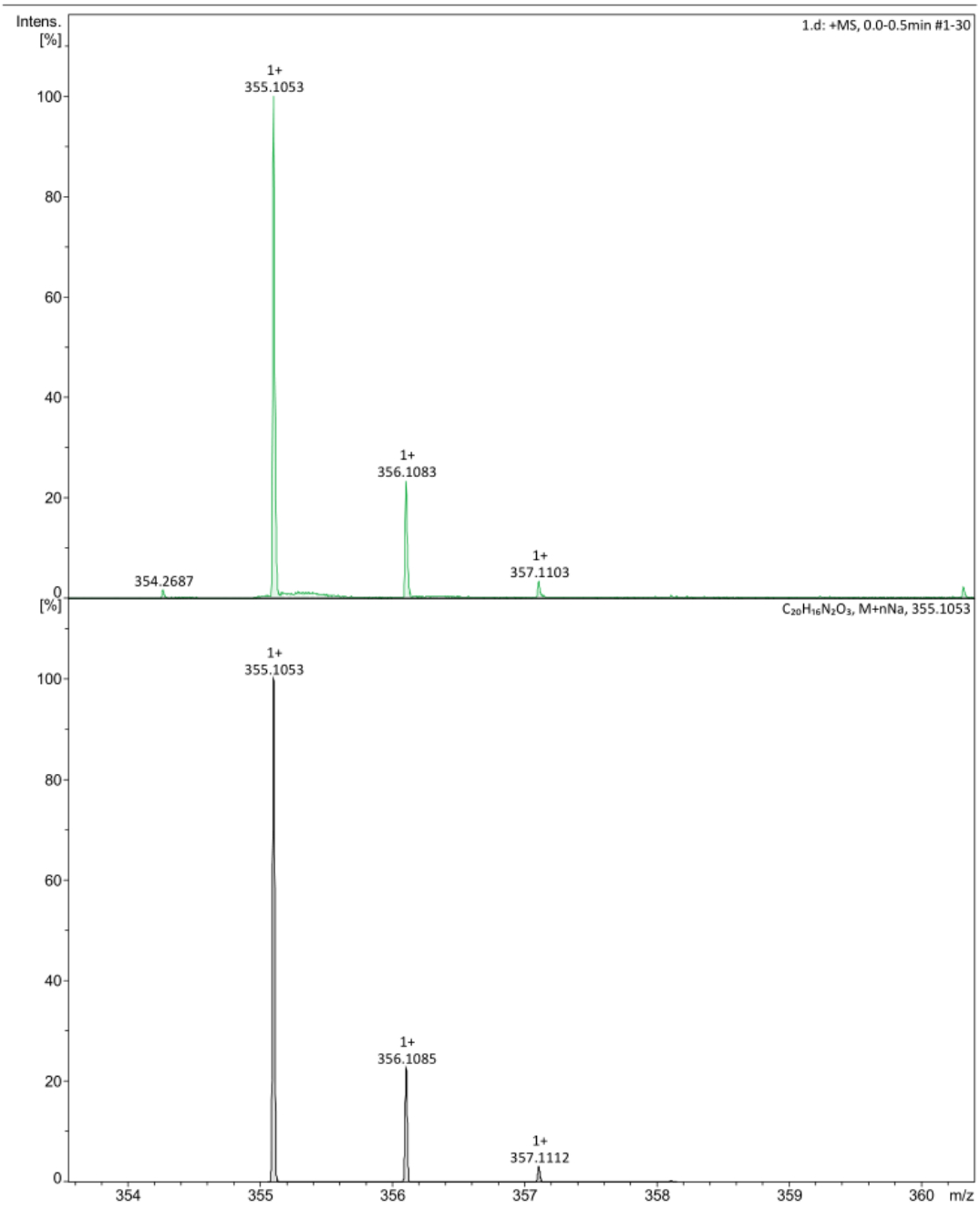


**Fig. S13** The HRMS spectrum of BP-NB.

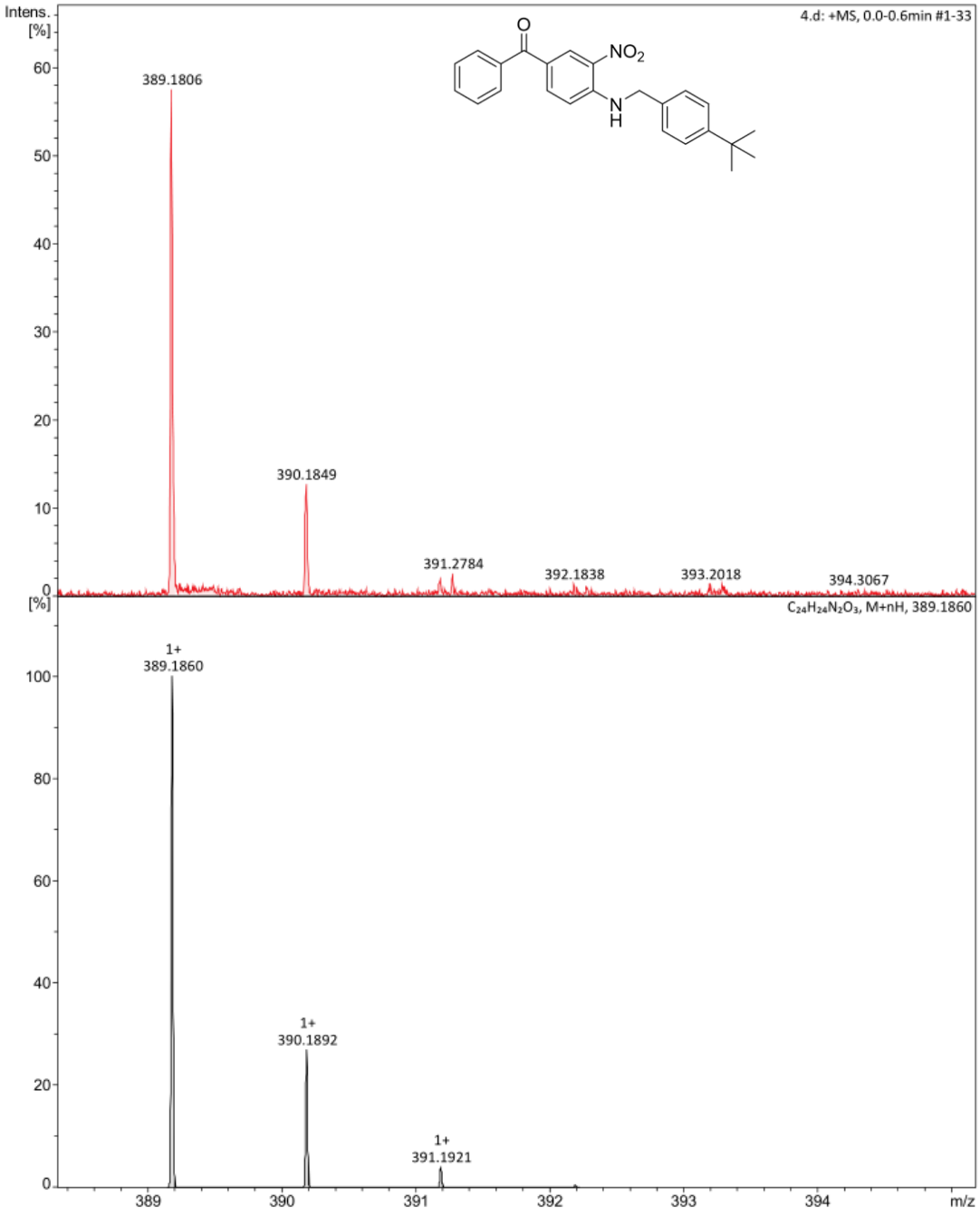


**Fig. S14** The HRMS spectrum of BP-NBtBu.

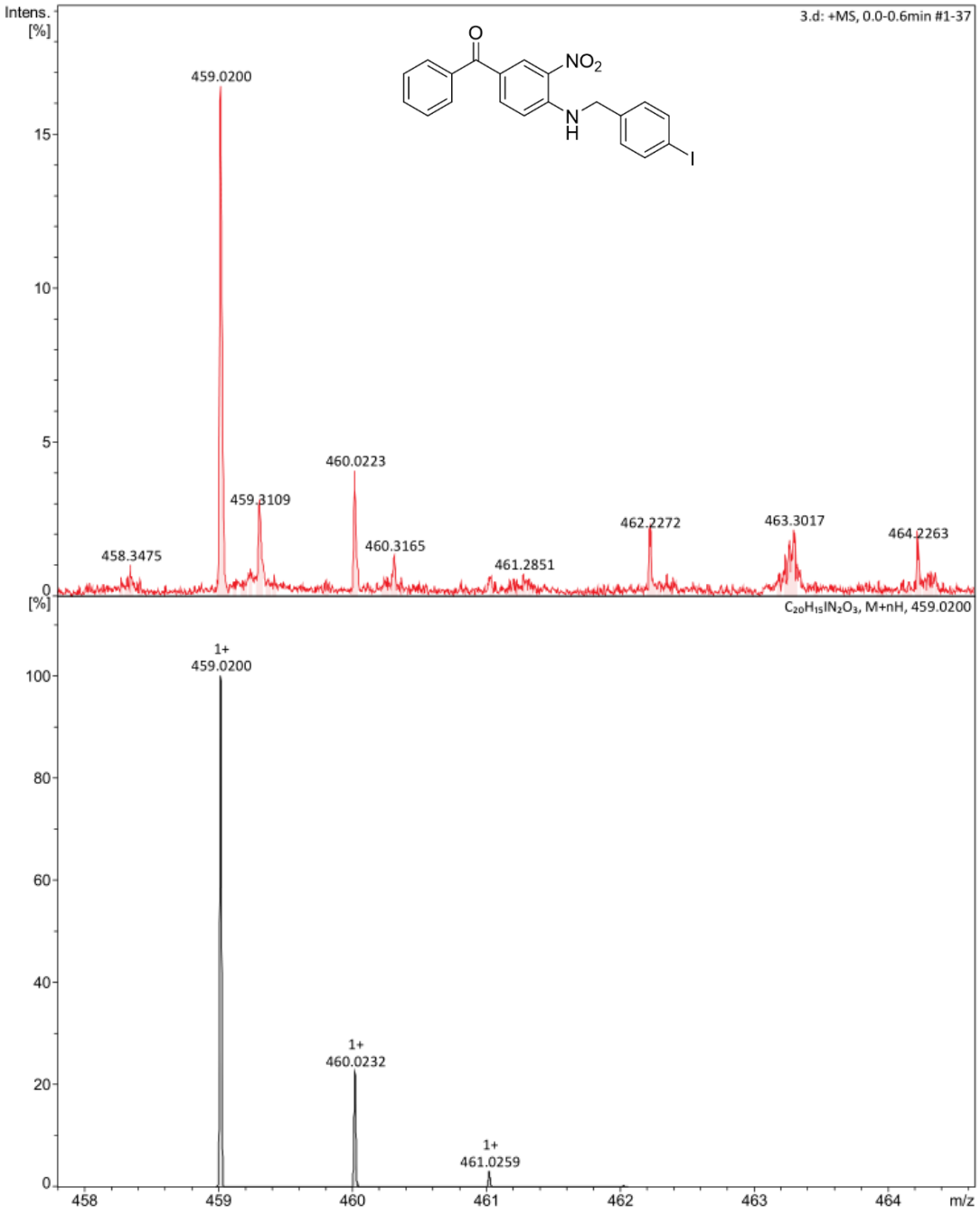


**Fig. S15** The HRMS spectrum of BP-NBI.

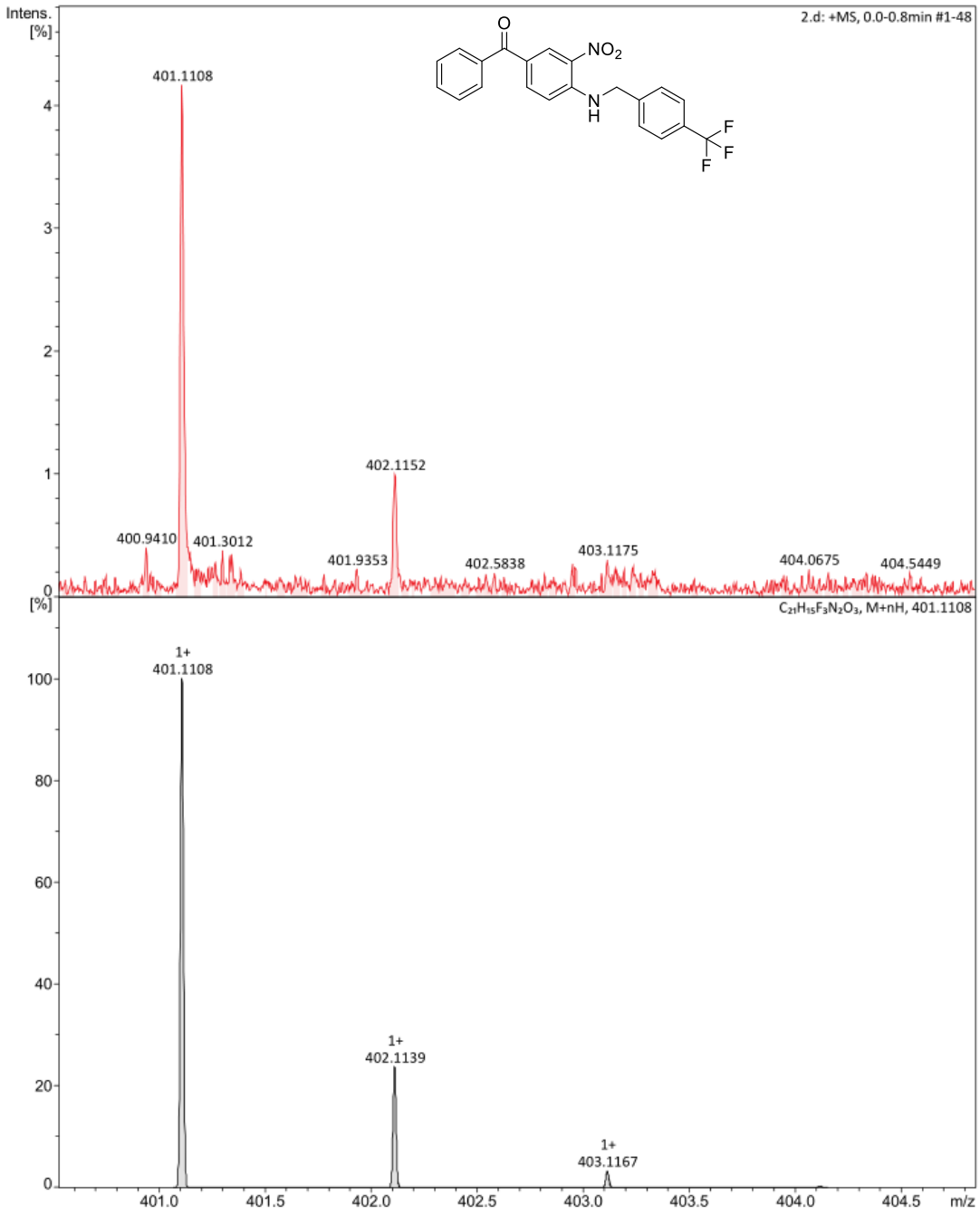


**Fig. S16** The HRMS spectrum of BP-NBCF$_3$.

## 2.2 Computational methods

To establish a reliable computational protocol, we performed a systematic benchmark of several density functionals (including PBEPBE, M062X, B3LYP, CAM-B3LYP, B3PW91, and mPW1PW91) in conjunction with basis sets of increasing size (6-311g(d,p), def2-tzvp) by comparing the calculated UV-Vis absorption spectra of BPNB against experimental data (see Table S1). The experimental maximum absorption wavelength of BPNB is 413 nm. Given the presence of hydrogen bonding in our system, we incorporated empirical dispersion corrections (e.g., D3(BJ)) for functionals where necessary. The vibrational frequencies were further examined to ensure the obtained geometries are void of imaginary frequency. Their UV-visible spectrum was also calculated by the same method and basis sets as the geometry optimization. The benchmark results as shown in Fig. S17 indicate that the B3LYP/6-311g(d,p) level of theory offers the optimal results.

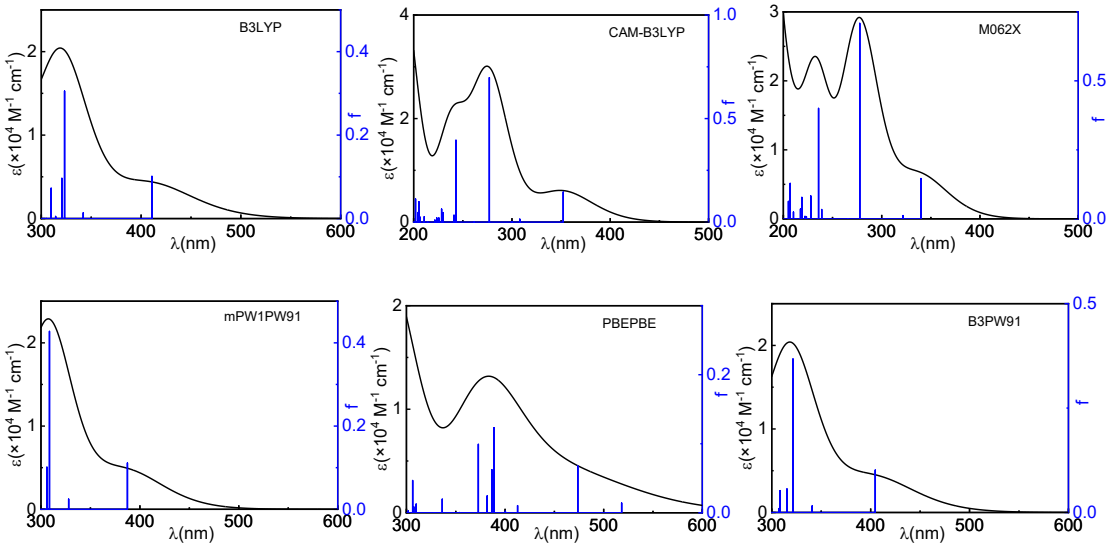


Fig. S17 The theoretical UV-visible absorption spectrum of BPNB and the oscillator strength of the related excited state in acetonitrile calculated by different functionals in combination with 6-311g(d,p), em=D3(BJ).

Table S1 The theoretical maximum absorption wavelength of BPNB in acetonitrile by different functionals in combination with basis sets of 6-311g(d,p), em=D3(BJ).

| Functionals | B3LYP | CAM-B3LYP | M062X | mPW1PW91 | PBEPBE | B3PW91 |
|---|---|---|---|---|---|---|
| $\lambda_{max}$/nm | 411 | 352 | 340 | 387 | 518 | 405 |

The theoretical UV-visible absorption spectrum of BPNB and the oscillator strength of the related excited state in acetonitrile calculated by B3LYP in combination with 6-311g(d,p) and def2tzvp, without set of em=D3(BJ) was shown in Fig. S18. The related data was shown in Table S2. From the comparison of the results shown in Table S1 and Table S2, the B3LYP/6-311g(d,p)

without set of em=D3(BJ) was the optimal compromise between computational cost and predictive accuracy.

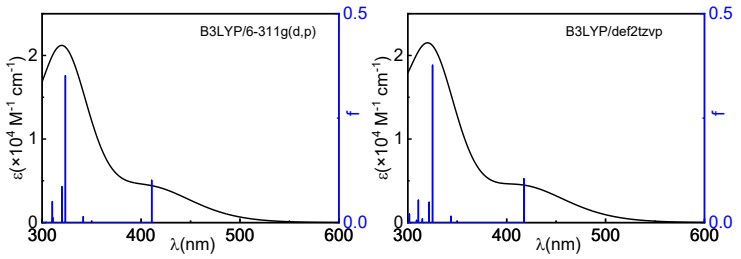


Fig. S18 The theoretical UV-visible absorption spectrum of BPNB and the oscillator strength of the related excited state in acetonitrile calculated by B3LYP in combination with 6-311g(d,p) and def2tzvp, without set of em=D3(BJ).

Table S2 The theoretical maximum absorption wavelength of BPNB in acetonitrile by B3LYP in combination with basis sets of 6-311g(d,p) and def2tzvp, without set of em=D3(BJ).

| Basis set | 6-311g(d,p) | Def2tzvp |
|---|---|---|
| $\lambda_{max}$/nm | 411 | 417 |

**2.3 TD-DFT data**

Table S3 TD-DFT data relative to their lowest energy electronic transitions.

| PIs | $S_v$/eV | $S_1$/eV | $T_1$/eV | $T_2$/eV | $\Delta E_{S1-T1}$/eV |
|---|---|---|---|---|---|
| BP-NB | 3.02 | 2.36 | 1.95 | 2.66 | 0.41 |
| BP-NBI | 3.02 | 2.37 | 1.96 | 2.66 | 0.41 |
| BP-NBtBu | 3.02 | 2.39 | 1.96 | 2.66 | 0.43 |
| BP-NBCF$_3$ | 3.03 | 2.37 | 1.97 | 2.66 | 0.41 |

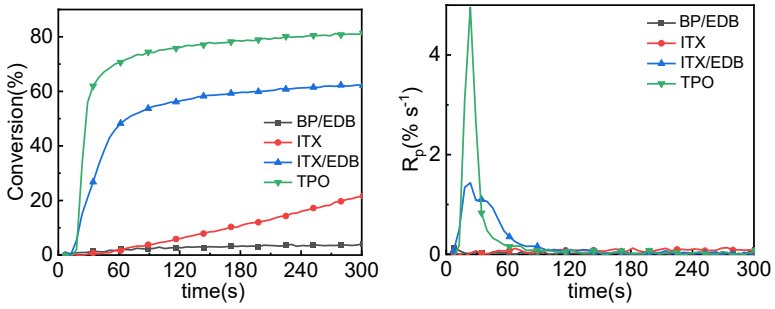


Fig. S19 Photopolymerization profiles of HDDA initiated by different photoinitiating systems upon LED@450nm exposure (I=140 mW cm$^{-2}$). [PI]=1%; [EDB]=3%.

Reference


1 Z. Lee, T. Huang, F. Hammoud, C. Chem. A. Hijazi, B. Graff, J. Lalevee and Y. Chen, Effect of the steric hindrance and branched substituents on visible phenylamine oxime ester photoinitiators: Photopolymerization kinetics investigation through photo-DSC experiments, *Photochem. Photobio.*, 2022, **98**, 773-782.

2 M. J. Frisch, *et al*. Gaussian 16, Revision A.03, Gaussian, Inc., Wallingford CT, 2016.

3 Q. Wu, J. Guo, K. Song, S. Xu, F. Li and M. Deng, Photoinitiation mechanism and ability of thioxanthone-based versatile visible photoinitiators, *Macro. Chem. Phys.*, 2022, **223**(23), 2200242.

4 Z. Liu, T. Lu and Q. Chen, An sp-hybridized all-carboatomic ring,cyclo[18]carbon: Electronic structure, electronic spectrum, and optical nonlinearity, *Carbon*, 2020, **165**, 461-467.

5 T. Lu and F. Chen, Multiwfn: A multifunctional wavefunction analyzer, *J. Comput. Chem.*, 2012, **33**(5), 580-592.

6 D. Rehm and A. Weller, Kinetics of fluorescence quenching by electron and H-atom transfer, *Isr. J. Chem.*, 1970, **8**, 259-271.

7 M. A. Tehfe, F. Dumur, B. Graff, D. Gigmes, J. P. Fouassier and J. Lalevee, Blue-to-red light sensitive push-pull structured photoinitiators: indanedione derivatives for radical and cationic photopolymerization reactions, *Macromolecules*, 2013, **46**(9), 3332-3341.